Universitat Autònoma de Barcelona

Dipòsit digital de documents de la UAB

This is the **accepted version** of the journal article:

Schaefer, Christian M.; Caicedo Roque, Jose Manuel; Sauthier, Guillaume; [et al.]. «Carbon incorporation in MOCVD of MoS2 thin films grown from an organosulfide precursor». Chemistry of materials, Vol. 33, Issue 12 (June 2021), p. 4474-4487. DOI 10.1021/acs.chemmater.1c00646

This version is available at https://ddd.uab.cat/record/266839

under the terms of the IN COPYRIGHT license

Carbon incorporation in MOCVD of MoS_2 thin films grown from organosulfide precursor

Christian M. Schaefer[1], José M. Caicedo Roque[1], Guillaume Sauthier[1], Jessica Bousquet[1†], Clément Hébert[1#], Justin R. Sperling[1], Amador Pérez-Tomás[1], José Santiso[1], Elena del Corro[1], Jose A. Garrido[1,2*]

[1]Catalan Institute of Nanoscience and Nanotechnology (ICN2), CSIC and BIST, Campus UAB, 08193 Bellaterra, Spain

[2]ICREA, 08010 Barcelona, Spain

ABSTRACT: With the rise of two-dimensional (2D) transition-metal dichalcogenide (TMD) semiconductors and their prospective use in commercial (opto)electronic applications, it has become key to develop scalable and reliable TMD synthesis methods with well monitored and controlled levels of impurities. While metal-organic chemical vapor deposition (MOCVD) has emerged as the method of choice for large-scale TMD fabrication, carbon (C) incorporation arising during MOCVD growth of TMDs has been a persistent concern – especially in instances where organic chalcogen precursors are desired as a less hazardous alternative to more toxic chalcogen hydrides. However, the underlying mechanisms of such unintentional C incorporation and the effects on film growth and properties are still elusive. Here, we report on the role of C-containing side-products of organosulfur precursor pyrolysis in MoS_2 thin films grown from molybdenum hexacarbonyl $Mo(CO)_6$ and diethyl sulfide $(CH_3CH_2)_2S$ (DES). By combining *in situ* gas-phase monitoring with *ex situ* microscopy and spectroscopy analyses, we systematically investigate the effect of temperature and $Mo(CO)_6$:DES:H_2 gas mixture ratios on film morphology, chemical composition, and stoichiometry. Aiming at high-quality TMD growth, that typically requires elevated growth temperatures and high DES:$Mo(CO)_6$ precursor ratios, we observed that temperatures above DES pyrolysis onset ($\gtrsim$600ºC) and excessive DES flow result in the formation of nanographitic carbon, competing with MoS_2 growth. We found that by introducing H_2 gas to the process DES pyrolysis is significantly hindered, which reduces carbon incorporation. The C content in the MoS_2 films is shown to quench the MoS_2 photoluminescence and influence the trion-to-exciton ratio via charge transfer. This finding is fundamental for understanding process-induced C impurity doping in MOCVD-grown 2D semiconductors and might have important implications for the functionality and performance of (opto)electronic devices.

I. Introduction

In recent years, two-dimensional (2D) materials beyond graphene have attracted great attention in fundamental and application-oriented research. Layered transition-metal dichalcogenides (TMDs), in particular, have become a forefront of 2D material research[1] due to their unique optoelectronic properties, such as layer-dependent tunable bandgap with indirect-to-direct bandgap transition in the monolayer limit,[2] and intense photoluminescence.[3] The semiconducting TMDs (e.g. MoS_2, WS_2, and WSe_2) are especially suitable for (opto)electronic applications, like low-power transistors with high ON/OFF-ratios,[4] logic-in-memory devices,[5] memtransistors for neuromorphic computing,[6] and neural network photodiode arrays.[7] Furthermore, TMDs have been used in a growing number of flexible devices, like rectennas,[8] photodetectors,[9] and wearable active-matrix light-emitting diodes.[10] The drive to fully take advantage of TMDs by successfully integrating them into commercial devices has resulted in a pressing demand for obtaining high-quality, electronic-grade TMDs with homogeneous film continuity on large surfaces.[11]

Both top-down (e.g. mechanical or chemical exfoliation from natural bulk crystals) and bottom-up (e.g. synthetic vapor phase methods) have been used to produce TMDs.[12] While bulk exfoliation via the scotch tape method has been widely used in laboratories to isolate and integrate pristine TMD layers into proof-of-concept devices with high electronic performance,[4] this method is not suitable for commercial batch fabrication, which requires a scalable, controllable, and reproducible manufacturing process. Therefore, extensive efforts have led to the development of a variety of vapor phase techniques, as reviewed elsewhere.[1] Metal-organic chemical vapor deposition (MOCVD), an established manufacturing method for traditional compound semiconductors,[13] is one of the most promising candidates to meet the aforementioned industrial criteria for large-area and high-throughput TMD growth.[14-16] MOCVD

relies on a precise and independent supply of gaseous precursors into a heated reaction zone, which enables strict control over vapor-phase chemistry. This process can yield continuous and uniform deposition of atomically thin TMD films at wafer-scale[17] with layer-by-layer thickness control.[18]

Yet, there are still open questions about optimal MOCVD synthesis conditions depending on precursor chemistry,[19] and, in particular, the chosen chalcogen precursor (i.e. the S or Se source).[14, 20, 21] While carbon-free chalcogen hydrides (H_2S or H_2Se) are viable precursors for TMD growth according to thermodynamic predictions[22, 23] and experimental studies,[11, 24, 25] cost and safety considerations[26] have motivated further research into their low-cost and less harmful organic counterparts, such as dimethyl sulfide $(CH_3)_2S$,[18, 27, 28] diethyl sulfide $(CH_3CH_2)_2S$,[17, 24, 29-31] diethyl disulfide $(CH_3CH_2)_2S_2$,[15, 16] di-*tert*-butyl sulfide $((CH_3)_3C)_2S$,[32-34] and dimethyl selenide $(CH_3)_2Se$.[35, 36] Among these chalcogen sources, diethyl sulfide (DES) has become a popular precursor choice after the pioneering work of *Kang et al,*[17] and, as such, is used in our work as representative for the variety of organic chalcogen precursors. However, the use of DES brings new challenges as carbon (C) can be introduced as an unintentional film impurity due to pyrolysis side-products from organic ligands.[24, 36, 37] Currently, there is an ongoing discussion about the location and chemical nature of such C impurities and their influence on film growth and properties. Some researchers observed co-deposited 'amorphous carbon'[38] or 'defective graphene'[36] to form simultaneously with the TMD layer at the substrate/TMD interface, sensitively impeding the lateral 2D growth and TMD film quality characteristics like grain size, continuity, phase purity and stoichiometry.[24, 36] Other researchers describe C incorporation into synthetic TMD crystals, such as by substitutional C doping[39] or CH functionalization[40, 41] at chalcogen sites of the TMD basal plane, or by carbide transformation of TMD edges.[42] The latter edge carbidization of MoS_2 catalysts is a known phenomenon in the field of hydrodesulfurization.[43] The edge termination dictates grain morphology and is sensitively modified by the H_2/H_2S gas-phase environment[44, 45] and the sulfiding agent.[20, 21] While sulfidation with H_2S is reported to yield thermodynamically favored triangular MoS_2 grain shape,[20, 24] the use of organosulfides can disturb crystallinity,[20, 24] although the role of carbonaceous species has not been fully understood. Additional to their effect on film growth and morphology, C impurities were reported to alter the (opto)electronic properties of TMD films; if used in a controlled manner, C doping might be a route to tailor electronic TMD devices by synthetic means.[40] On the other hand, unintentionally introduced C impurities might have unwanted consequences, such as quenched photoluminescence,[24, 39] and shift of film properties from semiconducting to conducting resulting in impaired ON/OFF transistor performance.[38, 46] Thus, the C impurity concentration in TMD films is an important quality metric that needs to be controlled. Although several strategies have been applied to mitigate C incorporation, e. g. using alkali-assisted synthesis[38] and adding reductive H_2 gas to the growth process,[22-24, 32, 35, 38] common practice in these studies relied only on post-growth film characterization as a qualitative guide for process optimization. At present, little effort has been devoted to include *in situ* gas-phase monitoring and a quantitative approach that systematically relates C content with MOCVD growth conditions. Consequently, a comprehensive view on the origin and influence of C incorporation is still elusive. Moreover, the role of different reactor setups, e.g. hot-wall and cold-wall configurations, and their impact on C formation rate is still under debate.[24] Therefore, it is crucial to understand the underlying organosulfur precursor pyrolysis to control impurity introduction, which potentially results in doping effects,[47, 48] and, eventually, to find appropriate process windows for films with desired properties.

In this work, we investigate the growth of MoS_2 on SiO_2/Si by MOCVD in a hot-wall reactor from molybdenum hexacarbonyl $Mo(CO)_6$ and the organic chalcogen precursor diethyl sulfide [DES; $(CH_3CH_2)_2S$], exploring the impact of the growth parameters on the C incorporation. By employing *in situ* gas-phase analysis with a mass spectrometer, we systematically study synthesis conditions for single and multi-source DES, $Mo(CO)_6$, DES:$Mo(CO)_6$ and DES:$Mo(CO)_6$:H_2 gas mixtures and varied temperatures. We reveal that DES pyrolysis, via an unimolecular dissociation pathway, releases carbonaceous gas-phase constituents, resulting in co-deposited C as a competing side-product to MoS_2 growth. Using extensive *ex situ* characterization, such as scanning electron microscopy (SEM), atomic force microscopy (AFM), semi-quantitative Raman spectroscopy, X-ray photoelectron spectroscopy (XPS), and photoluminescence (PL) spectroscopy, we elucidate the effect of C on the MoS_2 film morphology, chemical composition, stoichiometry, and electronic doping. Our work identifies these film properties to be highly interrelated with C incorporation, which underlines the significance of controlling C impurity levels during MOCVD.

II. Experimental Section & Methods

MoS_2 synthesis. MoS_2 films were grown by metal-organic chemical vapor deposition (MOCVD) in a home-built, hot-wall reactor (Figure S1). First, 285 nm SiO_2 grown on Si wafers were diced into 1x1 cm² chips and sonicated in 3:1 piranha solution (conc. H_2SO_4: H_2O_2 35 wt%) for 15 min, thoroughly rinsed with deionized water, and blow-dried with N_2. Substrates were placed face-down onto a quartz sample holder bar that was introduced into the vertical quartz tube reactor chamber. A thermocouple and temperature controller were used to measure and set the temperature at the sample, referred to as "growth temperature". Following the growth process outlined in Figure S2a, the reactor was ramped to the desired growth temperature at a rate of around 40 °C/min under inert purge gas flow of 100 sccm high-purity Ar (Air Liquide, Alphagaz™ 1, 99.999%). Then, Ar was switched off and MoS_2 growth was initiated by vapor draw of molybdenum hexacarbonyl $Mo(CO)_6$ (Sigma Aldrich 577766, >99.9 % trace metal basis) and $(C_2H_5)_2S$ (DES, Sigma Aldrich 107247, 98 %) from

dedicated canisters without any carrier gas. $Mo(CO)_6$ powder bedded on glass beads for high surface area[12, 49] and DES precursors were held at 30°C and 12 °C, respectively, and their flow was independently regulated by needle metering valves (SS-SS4-VH, Swagelok) and estimated based on equilibrium vapor pressure data, as described in the Supporting Information (Figure S3). Nominal $Mo(CO)_6$ flows of 0.02 sccm and DES flows between 0.3 and 13.2 sccm were used. Additionally, high purity H_2 gas (Air Liquide, Alphagaz™ 1, 99.999%) with flows between 0 – 30 sccm was injected with a mass flow controller from a separate line. Typical working pressures were in the range of 10^{-2} to 10^{-1} torr. Growth was stopped by cutting the $Mo(CO)_6$, DES and H_2 flow; then, the reactor was cooled down to room temperature under 100 sccm Ar flow before sample removal. After each run, the reactor was annealed at 800 °C in flowing Ar/H_2 flow to remove residual reaction products (Figure S2b), and between runs was held under vacuum at around 1×10^{-3} torr base pressure. During sample loading/unloading 150 sccm Ar was flowed to minimize ambient exposure of the tube. Samples were stored in a vacuum desiccator.

SEM analysis. The film morphology was analyzed by high-resolution field-emission Scanning Electron Microscopy (SEM) in immersion mode with a FEI Magellan 400L XHR at low accelerating voltages of 2 kV and 100 pA beam current at a working distance of 3.8 mm. A sample bias of 4 kV was used to compensate charging of the insulating substrate and a vCD-detector was used for high contrast imaging of back-scattered electrons at low voltages. SEM images were analyzed with the open-source program ImageJ 1.51j8.[50] An image analysis algorithm was used that converts the SEM to binary images from the grain-substrate contrast and applies the "analyze particles" tool to extract film coverage and nucleation density. Film coverage θ was determined as the percentage of covered substrate area, and the nucleation density was determined as the counted MoS_2 grains per unit area of the SEM image. More details are given in the Supporting Information (Figure S4).

Raman and PL spectroscopy. As-grown films were characterized under ambient conditions with a confocal Witec alpha300R A300M+ microscope at 100x magnification by using a laser with 488 nm excitation wavelength and spot size of around 1 µm. A low laser power of 0.2 mW was used to minimize laser heating effects and avoid optical doping and multiexciton dynamics in the PL measurements.[51] Integration times of 5 s and two accumulations were used for all measurements. For each sample three spots were measured along the sample diagonal for averaged data and corresponding standard deviations as statistical errors. Witec PROJECT 5.0 software was used for peak fitting and analysis.

E^1_{2g} and A_{1g} Raman modes of MoS_2, Si and carbon D and G bands were measured with a 600 grooves/mm diffraction grating within the same spectral window. For semi-quantitative Raman integral analysis MoS_2 bands were fitted with double Lorentzians, Si bands with single Lorentzians, and the carbon D and G bands with Double-Gaussians after first order background subtraction. Within our fitting strategy we used a boundary condition to exclude the contribution of a peak appearing in the low frequency shoulder of the D peak and that we were not able to correlate to the growth conditions. Crystallite size L_a of graphitic carbon was estimated from the intensity ratio of D and G peaks by the relation $L_a = 560/E_l^4\ (I_D/I_G)^{-1}$, where E_l is the excitation laser energy 2.54 eV.[52] For precise analysis of A_{1g} and E^1_{2g} peak positions and determination of the frequency difference $\Delta(A_{1g}\text{-}E^1_{2g})$ a high resolution 1800 grooves/mm grating was used.

For PL measurements a 600 grooves/mm grating was used. After background subtraction, Lorentzian peak fitting was performed to account for the charged trion A^-, neutral exciton A^0, and B exciton contributions. Fitting constraints for peak positions were chosen according to literature data (see Table S2). To ensure comparability between samples the PL intensity is defined by the relative $(A^-+A^0)/B$ intensity ratio,[53] which is the peak integral ratio of summed A^- and A^0 contributions with respect to the B exciton.

XPS analysis. The chemical composition and stoichiometry of the films was investigated by X-ray Photoelectron Spectroscopy (XPS) in ultra-high vacuum of 5×10^{-10} mbar with a SPECS PHOIBOS 150 hemispherical analyzer by using monochromatic Al Kα radiation with an energy of 1486.6 eV. To compensate for sample charging all spectra were energy corrected against the Si 2p reference peak of the thermally oxidized SiO_2/Si substrate. Details about the fitting procedure and constraints are given in the Supporting Information (Table S1).

Mass spectroscopy. A Hiden Analytical HPR-30 residual gas analyzer equipped with a triple filter quadrupole mass spectrometer was used for *in situ* gas-phase analysis. The gas analyzer was connected downstream from the MOCVD tube furnace via a sampling needle valve (Figure S1b) and the pressure inside the mass spectrometer was set to 10^{-6} torr. Soft electron ionization at low electron emission energy of 12 eV and 100 µA emission current was used to minimize electron-ionization-induced fragmentation of the DES molecular ion and for selective detection of DES pyrolysis products. A secondary electron multiplier detector was used for high sensitivity detection at acquisition range of 10^{-11} torr. For the temperature dependent DES pyrolysis study the reactor temperature was ramped with 10 °C/min from room temperature to 800 °C while introducing different $DES:Mo(CO)_6:H_2$ mixtures and continuously monitoring the partial pressure of gas-phase constituents, e.g. the unfragmented DES molecular ion (m/z=90) and main pyrolysis products, such as ethyl radicals (m/z=29) and ethylene (m/z=28). Selective ionization of ethylene is ensured by the low ionization energy, which avoids formation of isobaric ions of N_2 and CO that require higher ionization energies than used in this experiment. This also means that H_2 could not be detected under these conditions due to its higher ionization energy.

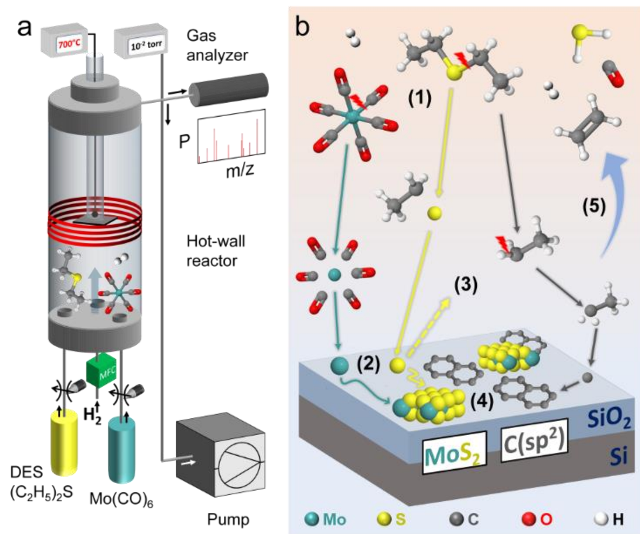

Figure 1. a) Schematic of the hot-wall MOCVD reactor. Controlled precursor flows of molybdenum hexacarbonyl $Mo(CO)_6$ and diethyl sulfide [DES; $(CH_3CH_2)_2S$] are injected from external canisters together with H_2 into the reaction zone at growth temperatures from 550°C to 800°C and pressure of ca. 10^{-2} to 10^{-1} torr. *In situ* gas-phase monitoring of the reaction and pyrolysis products is enabled by a gas analyzer (mass spectrometer) attached downstream the reaction zone. b) Simplified illustration of the MOCVD process, involving (1) precursor decomposition, (2) surface adsorption and diffusion, (3) desorption, (4) growth of MoS_2 and graphitic C(sp²) domains on the SiO_2/Si substrate surface, and (5) release of gaseous by-products.

III. Results & Discussion

This study focuses on the MOCVD growth of atomically-thin MoS_2 films from gas-source precursors in a vertical hot-wall reactor, as depicted in Figure 1a. Low pressure conditions (10^{-2} – 10^{-1} torr) were chosen for vapor draw transport of the Mo and S precursors into the reaction chamber without carrier gas and to promote surface reactions on the SiO_2/Si substrate. SiO_2/Si has been chosen because it is a technologically relevant substrate of the semiconductor industry, has been widely used for TMD synthesis due to its chemical inertness at high growth temperatures, and provides an ideal platform for optical characterization by means of Raman and PL spectroscopy.[54]

As it is difficult to capture the complex mechanisms in a holistic growth model, Figure 1b illustrates a simplified version of the MOCVD process, involving (1) thermal decomposition of $Mo(CO)_6$ and DES at high temperature, (2) adsorption and diffusion of Mo and S species on the SiO_2/Si substrate, (3) S desorption and (4) nucleation and lateral growth of atomically thin MoS_2 domains, with simultaneous incorporation of graphitic C(sp²), and (5) release of gaseous by-products, such as carbon monoxide CO, ethylene C_2H_4, hydrogen H_2, and hydrogen sulfide H_2S. In discussion of the growth model, we note that MOCVD reactions occur both in the gas-phase and on the surface.

Surface reactions involve physisorption and chemisorption processes,[55] and substrate-mediated precursor decomposition, such as the decarbonylation of $Mo(CO)_6$ on SiO_2.[56] The sulfidation of Mo adatoms results in the nucleation of MoS_2 domains, which grow laterally through edge attachment of additional Mo and S species.[16, 17] During sulfidation a sufficiently high chalcogen-to-metal ratio is an important parameter to avoid Mo accumulation and formation of Mo metal-rich clusters.[35] In our MOCVD setup, the DES:$Mo(CO)_6$ precursor ratio can be tuned by independent source control to achieve desired chalcogen-to-metal ratio on the surface. For stoichiometric TMD growth, a high chalcogen-to-metal ratio is typically required to compensate for the large discrepancy in vapor pressures, sticking coefficients, and diffusion kinetics of the chalcogen and the transition-metal species.[24, 35]

Gas-phase reactions include thermal decomposition (pyrolysis) of the precursors $Mo(CO)_6$[57] and DES[37], and also gas-phase reactions between them might be possible.[58] Our setup allows to monitor these gas-phase processes with a mass spectrometer connected to the reactor, and in this study we will particularly focus on the role of DES pyrolysis. DES pyrolysis becomes important at comparatively high growth temperatures of ≥600ºC and increased chalcogen-to-metal ratios, which have been reported to be favorable conditions for high-quality TMD growth with enhanced grain sizes.[14, 35, 49] However, these conditions can lead to disturbed MoS_2 growth due to the formation of graphitic C(sp²), that results from the carbonaceous by-products of DES pyrolysis.

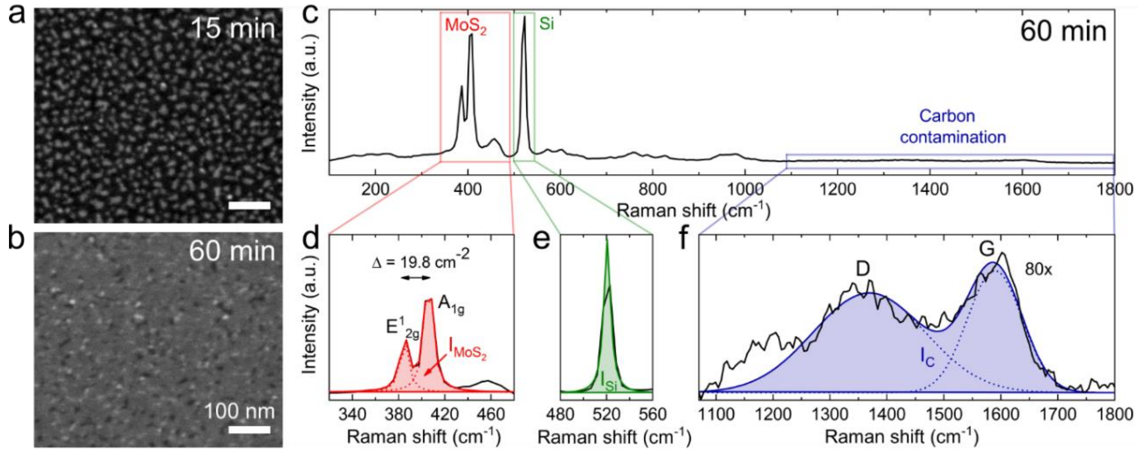

Figure 2. MoS_2 grown at 700ºC by co-injection of 0.3 sccm DES and 0.02 sccm $Mo(CO)_6$ precursor flow without reductive H_2 gas flow. a), b) SEM images of MoS_2 nuclei after 15 min, and of coalesced 1L-MoS_2 thin film after 60 min growth time, respectively. c) Raman spectrum of 1L-MoS_2 from b). (d-f) show the three regions of interest for semi-quantitative Raman analysis: d) MoS_2-related modes fitted with a double-Lorentzian, e) Si mode fitted with a single-Lorentzian, and f) C-related D and G bands fitted with a double-Gaussian and magnified by a factor of 80. The peak integrals for the Raman modes associated to MoS_2, Si and C are defined as I_{MoS2} (red), I_{Si} (green) and I_C (blue), respectively.

3.1 Assessment of MoS_2 film properties and C incorporation

In a first experiment MoS_2 was synthesized by co-injection of 0.3 sccm DES and 0.02 sccm $Mo(CO)_6$ at 700°C. Figure 2a and Figure 2b correspond to the SEM images of two films with growth times of 15 min and 60 min, respectively. The short 15 min growth allows assessment of the nucleation and lateral growth of monolayer MoS_2 domains (grey contrast) on SiO_2 (black contrast). The 60 min growth reveals a continuous monolayer (1L) film with minor second layer nucleation (white contrast spots). By increasing the growth time, few layer MoS_2 growth (>1L) was also achieved (Figure S5). However, in this paper we will focus on 0 – 1L films defined by 0 – 100% coverage θ. The high nucleation density of the first layer (~10^3 µm^{-2}), which has been observed consistently throughout this work (Figure S9), produces a nanocrystalline MoS_2 monolayer with small grain sizes (20 – 30 nm). This can be explained by high Mo flux controlled growth rates[16, 17, 59], high gas-phase supersaturation at low reactor pressure,[22, 35] and low diffusivity of surface species due to hydroxyl anchoring sites on the SiO_2 substrate.[60] While large grain sizes (>µm scale) are typically desired for high performance (opto)electronic applications, the focus of our investigation was on the origin and effect of C incorporation instead of grain size, as previous works have already addressed the suppression of nucleation density, e. g. by alkali-catalyzed synthesis.[38, 49]

Figures 2(c-f) show an exemplary Raman spectrum of the coalesced 1L-MoS_2 film and the three Raman regions of interest. Figure 2d represents the prominent Raman-active E^1_{2g} and A_{1g} bands at 382.6 cm^{-1} and 402.4 cm^{-1} of the in- and out-of-plane phonon modes, respectively, corresponding to the thermodynamically stable 2H-phase of MoS_2. The full-width-at-half maximum (FWHM) of E^1_{2g} and A_{1g} peaks are 5.7 cm^{-1} and 5.0 cm^{-1}, respectively. The frequency difference Δ = 19.8 cm^{-1} between the E^1_{2g} and A_{1g} modes, commonly used as a layer-thickness indicator, confirms the monolayer thickness of the film.[18, 61] Figure 2e shows the Si band at 521 cm^{-1} from the growth substrate and Figure 2f reveals broad D and G modes at around 1360 cm^{-1} and 1590 cm^{-1} due to the presence of C incorporation in the film.[24, 36] Based on the D and G peak positions and an integrated I_D/I_G intensity ratio of around 1.7, this Raman signature is assigned (as confirmed by the XPS analysis below), to sp^2 carbon, such as pyrolytic graphite,[62] with an estimated crystallite size below 10 nm.[52] The nanographitic film can possibly contain a low fraction of amorphous C(sp^3), according to the amorphization trajectory of disordered C proposed by Ferrari *et. al*.[63] Notably, this result is consistent with a previous report on nanoscale nuclei of highly defective graphene as side product of TMD growth using an organic chalcogen source.[36]

For further evaluation of Raman spectra, peak fits were applied to the MoS_2, Si, and C bands. The respective peak integrals in Figure 2(d-f) are specified as $I_{MoS_2} = I_{E^1_{2g}} + I_{A_{1g}}$, I_{Si}, and $I_C = I_D + I_G$. By using the Raman integral ratios I_{MoS_2}/I_{Si} and I_C/I_{Si} as the indicators for monitoring the content of MoS_2 and co-deposited C(sp^2), respectively, we can employ Raman spectroscopy as a non-destructive tool for semi-quantitative characterization and comprehensive monitoring of trends in the growth parameter space (Figure S18). In the following, it will be employed to elucidate the effects of DES:$Mo(CO)_6$ ratio, growth temperature, and H_2 gas flow on MoS_2 growth and C incorporation. This method, which relies on a prominent substrate reference peak, makes SiO_2/Si an ideal choice for the growth surface in this study.

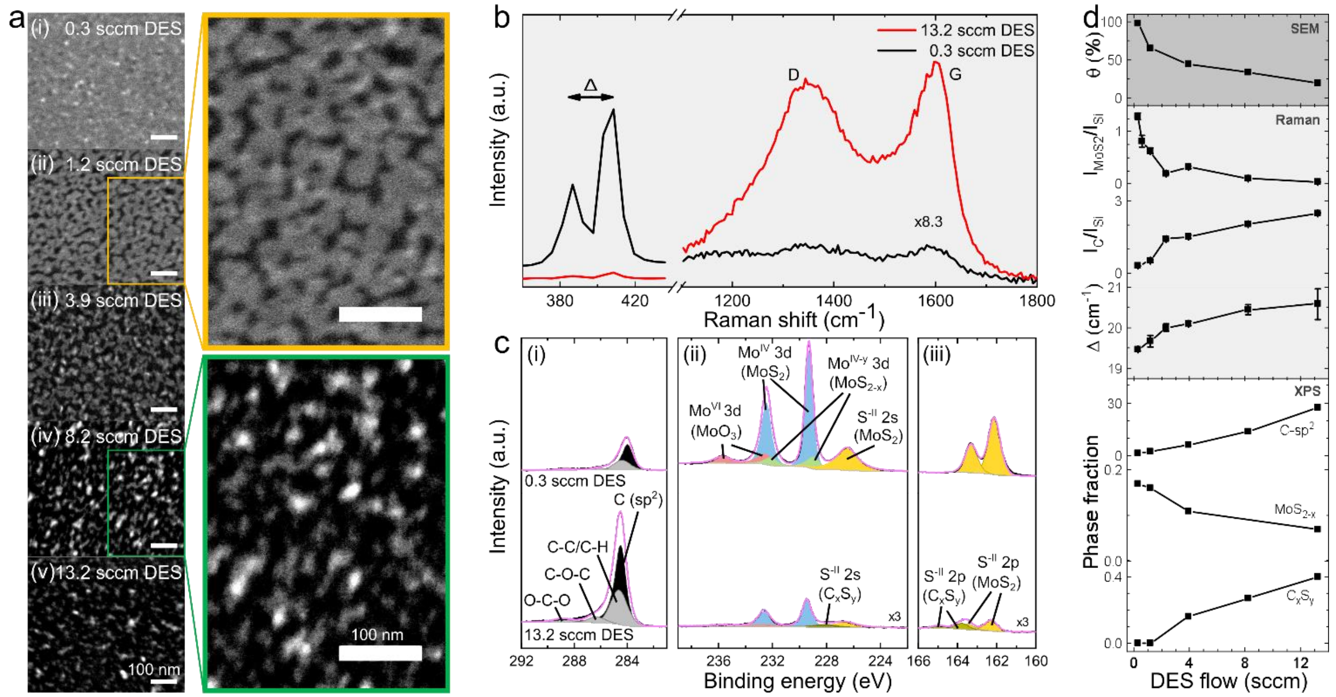

Figure 3. Effect of DES flow on MoS_2 thin films grown at 700°C (60 min) from 0.02 sccm $Mo(CO)_6$ and DES flow varying between 0.3 and 13.2 sccm. a(i-v) SEM images for different DES flows, as indicated in the figures. The insets show magnified images for better visualization of the grain morphology. b) Raman spectra normalized to Si peak (521 cm^{-1}, not shown) for 0.3 sccm (black) and 13.2 sccm (red) DES flow. The C-related D and G bands were magnified by a factor of 8.3. c(i-iii) XPS spectra for 0.3 sccm (top) and 13.2 sccm (bottom) DES flow of the C 1s, Mo 3d/S 2s and S 2p core levels; colored areas under singlet/doublet peaks represent fits assigned to the same chemical compound and pink lines show the fitting envelopes of summed peaks. d) Summary of film properties as a function of DES flow, coverage θ from SEM, Raman I_{MoS2}/I_{Si} and I_C/I_{Si} integral ratios, $\Delta(A_{1g}-E^1_{2g})$ frequency difference) and XPS sp²-C, MoS_{2-x} and C_xS_y fractions (normalized to MoS_2-related Mo^{IV} $3d_{5/2}$ peak).

3.2 Effect of DES:$Mo(CO)_6$ ratio

To study the effect of S:Mo ratio, MoS_2 films were grown at a constant temperature of 700ºC, growth time of 60 min and 0.02 sccm $Mo(CO)_6$ flow. The DES flow was varied from 0.3 sccm to 13.2 sccm, which corresponds to a variation of the DES:$Mo(CO)_6$ ratio from ~15 to ~660. SEM images (Figure 3a) and analysis (Figure 3d, 'SEM') reveal that as DES flow increases, the MoS_2 film coverage on the SiO_2/Si substrate monotonically decreases from 98% (i.e. a virtually closed 1L- MoS_2 film) to 19% at roughly constant nucleation density. Further, the shape of the MoS_2 grains becomes more irregular and rugged with increasing DES flow, as revealed by the insets in Figure 3a. The corresponding Raman spectra of these films (Figure 3b) show vanishing MoS_2 Raman E^1_{2g} and A_{1g} modes and growing D and G carbon bands with increasing DES flow (see Figure S17 for the complete set of Raman spectra of all DES flows). The Raman-based quantification method described in Section 2.1 allows us to monitor how the DES flow increase leads to a decreasing I_{MoS_2}/I_{Si}, and an increasing I_C/I_{Si} (Figure 3d, 'Raman', top and middle). This suggests that the C contamination introduced at high DES flow competes with and hinders the lateral MoS_2 growth, which explains the interrupted film morphology. Moreover, the MoS_2 layer thickness indicator $\Delta(A_{1g}-E^1_{2g})$, increases despite the reducing MoS_2 surface coverage (Figure 3d, 'Raman', bottom), suggesting a transition from a lateral growth of MoS2 domains to a vertical, layer-stacked MoS2 growth on existing domains. Topographical analysis by atomic force microscopy confirms this tendency by revealing particle formation with maximum heights up to ~4 nm and a monotonic increase of the root-mean-square roughness from 0.3 nm to 1.1 nm as the DES flow increases (Figure S10). As previously suggested, we speculate that the high energy SiO_2 surface preferred for lateral MoS_2 growth becomes increasingly covered by the co-deposited, low surface energy graphitic C, impeding the 2D lateral growth of MoS_2 domains and disturbing film coalescence. Thus, the presence of carbon can lead to interrupted TMD film continuity, in agreement with literature.[36, 59]

The morphological analysis by SEM and AFM might suggest the formation of an amorphous agglomerate of MoS_x phase instead of crystalline 2H-MoS_2 for the high DES flows. However, such an amorphous phase, like MoS_3, is reported to be thermally unstable and known to transform to crystalline 2H-MoS_2 above ~400°C[64, 65] The high growth temperature of 700°C used in this study should therefore

favor crystallization. Furthermore, the XPS data do not reveal any MoS_x-related peaks,[66] but rather suggests that there are changes in stoichiometry of the 2H-MoS_2 crystalline phase and film composition, as will be discussed in the following.

For comparison purposes, Figure 3c shows the XPS spectra corresponding to 0.3 sccm (top) and 13.2 sccm (bottom) DES flow (see Figure S12 for the complete set of XPS spectra of all DES flows). The high-resolution core level spectra of Mo 3d in Figure 3c(ii) reveal three types of Mo species of different oxidation states; each has been fitted with a doublet to obtain a satisfying deconvolution of the peak shape. The most prominent doublet, the blue colored area in Figure 3c(ii), is attributed to the Mo^{IV} oxidation state and corresponds to stoichiometric MoS_2, with the Mo $3d^{5/2}$ and Mo $3d^{3/2}$ spin-orbit components positioned at 229.3±0.1 eV and 232.5±0.1 eV, respectively. These binding energies are in agreement with literature values for MOCVD-grown MoS_2.[15] The higher binding energy doublet observed at 232.5±0.2 eV and 235.6±0.2 eV, attributed to the Mo^{VI} oxidation state ascribed to MoO_3, is present in all samples; it has been previously discussed in terms of post-growth oxidation of as-grown, chalcogen-deficient TMD films upon air exposure,[24] and it was also encountered in aged, natural MoS_2 crystals.[67] Although the growth was carried out in vacuum conditions, the observed low background levels of water in the reaction chamber, as monitored with mass spectroscopy (Figure S14), could eventually result in a partial oxidation during the growth.[68] The third doublet, observed at lower binding energy (within slight shifts at 229.0±0.2 eV and 232.2±0.2 eV), is attributed to the Mo^{IV-y} oxidation state related to a defective, substoichiometric MoS_{2-x} phase, where the exact position of the doublet depends on MoS_{2-x} stoichiometry.[69] The presence of this substoichiometric phase can be explained by S-vacancies due to incomplete sulfidation during the deposition process, a common observation in CVD-grown MoS_2.[70] The S:Mo stoichiometry of this S-deficient phase fraction can be estimated to lie between 1.6 and 1.9 based on the Mo $3d^{5/2}$ peak position.[69] Upon increasing the DES flow from 0.3 sccm to 13.2 sccm the fraction of the substoichiometric MoS_{2-x} (Mo^{IV-y} $3d^{5/2}$ area) in relation to ideal, stoichiometric MoS_2 (Mo^{IV} $3d^{5/2}$ area) is reduced from 0.17 to 0.07, as shown in Figure 3c(iii). To make this evident, we present a magnified view of the MoS_{2-x} peak evolution in the Supporting Information (Figure S12e). This result indicates that a higher DES flow (i.e. higher sulfidation potential) can lead to the deposition of MoS_2 films closer to the ideal stoichiometry relation.

However, as previously discussed, SEM and Raman analysis revealed that high DES flow results in co-deposited C, which hampers MoS_2 lateral growth, and, eventually, acts as an impurity. This conclusion is further supported by XPS, which shows an increase of the overall C 1s peak area (Figure 3c(i)) and a concurrent decrease of the Mo 3d peak area (Figure 3c(ii)) for increasing DES flows. XPS control experiments with *in situ* annealing (Figure S11) were performed to differentiate between adventitious C from post-growth ambient exposure (grey colored peak areas, Figure 3c(i)) and the growth-related C contributions, allowing us to identify the growth-induced C incorporation with its asymmetric C 1s peak at 284.2±0.2 eV as graphitic C(sp^2) (black colored area, Figure 3c(i)). The increase of DES flow from 0.3 sccm to 13.2 sccm results in an almost 20-fold increase of the fraction of co-deposited C(sp^2) (Figure 3d, 'XPS', top), resulting in heavily contaminated films. Further investigating the chemical nature of the C incorporation, we do not find evidence for the formation of possible C-Mo bondings, which would be apparent in the C 1s region at lower binding energies of around 282.8 eV.[42] Therefore, within the detection limit of our XPS study, we postulate that the C incorporation in our films is mainly composed of a graphitic C(sp^2) layer co-deposited with MoS_2 rather than substitutional doping of C into the MoS_2 sheet,[39] Mo_2C carbide formation,[28, 42] or CH groups at chalcogen sites previously reported in synthetic TMDs.[41] This agrees with the theoretical prediction that substitution of S with C atoms at the MoS_2 edge is thermodynamically unfavorable[20] and is further supported by the experimental observation that carbide conversion of MoS_2 does not occur below 800°C.[42]

Regarding the sulfur environment, we observe the characteristic MoS_2 fingerprints attributed to the S^{-II} oxidation state in accordance with literature[15]: a S 2p doublet at 162.1±0.1 eV and 163.3±0.1 eV, (Figure 3c(iii)) and a corresponding S 2s singlet peak at 226.5±0.1 eV (Figure 3c(ii)). Another S 2p doublet emerges at higher binding energies for DES flows above 3.9 sccm, positioned at 163.6±0.2 eV and 164.8±0.2 eV, as shown in Figure 3c(iii) for the 13.2 sccm DES flow. A similar S 2p doublet was previously observed in WS_2 growth using DES and was attributed to either S_xO_y oxysulfide or C_xS_y organosulfur compounds.[24] Analyzing our films we discard the presence of an intermediate MoS_xO_y oxysulfide phase, as the S 2p spectra do not show evidence of the distinct sulfur oxidation states characteristic of MoS_xO_y.[71] Instead, we assign the doublet to a C_xS_y organosulfur compound, whose content increases for high DES flow (Figure 3d, 'XPS', bottom, and Figure S12ef). Such organosulfur compounds were reported at binding energies of 163.7±0.3 eV[72] for sulfurized carbon black, activated carbon and charcoal, and in S-doped graphene.[73] Therefore, it is possible that these additional sulfur functionalities are incorporated into the carbonaceous film.

The overall trends seen in Figure 3d allow us to draw two significant conclusions. On the one hand, high DES:$Mo(CO)_6$ ratios are beneficial due to their high sulfidation potential, which helps reducing the fraction of the substoichiometric MoS_{2-x} phase (Figure 3d, 'XPS', middle). On the other hand, the high DES exposure conditions lead to a C-rich reaction environment that results in the deposition of graphitic C(sp^2), as well as in the incorporation of C_xS_y organosulfur compounds (Figure 3d, 'XPS', top and bottom), at the cost of MoS_2 growth. Therefore, the use of organic chalcogen precursors imposes a limitation on the maximum chalcogen-to-metal ratios as there is a clear trade-off between film stoichiometry and C incorporation.

3.3 DES pyrolysis as origin of C incorporation and effect of temperature

To clarify the origin of C incorporation into the films, SiO_2/Si samples were exposed only to a single source, either $Mo(CO)_6$ or DES, for 60 min at 700 ºC (Figure S13). While exposure to only $Mo(CO)_6$ yielded no D or G Raman bands characteristic for C(sp^2), samples exposed to only DES had intense D and G Raman signatures (I_C/I_{Si}=2.1). The lack of D and G Raman bands for the $Mo(CO)_6$ exposed samples was expected as the C-containing decomposition product of this precursor, CO, is regarded as an inert and thermally stable gas-phase compound; thus, it is not expected to participate in side-reactions that could lead to C incorporation under the used temperature conditions.[22, 32, 37] Therefore, DES is unequivocally identified as the source of C incorporation, which is consistent with previous reports of TMD growth processes using organic chalcogen precursors.[28, 32, 36] To further explore the role of DES as a source of C incorporation, single-source DES exposure of the SiO_2 surface was studied as function of growth temperature. As evident from Figure 4a, there is a rising intensity of the D and G bands with increasing temperature. We explain this observation by thermally activated decomposition (pyrolysis) of the organosulfide source as the underlying mechanism for C incorporation, in agreement with previous studies;[24, 36] and we go one step further to explicitly assess this occurrence in an MOCVD environment.

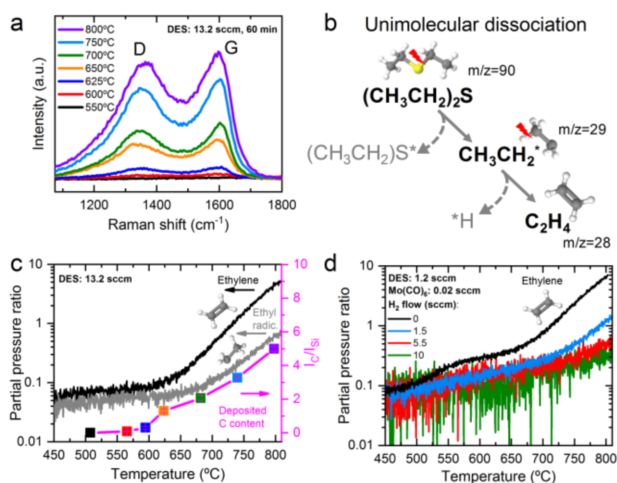

Figure 4. DES pyrolysis and C deposition for varying temperature and H_2 content. a) Raman spectra for single source exposure of SiO_2 substrates with 13.2 sccm DES for 60 min at temperatures ranging from 550ºC to 800ºC. b) Unimolecular dissociation pathway of DES pyrolysis, involving production of ethyl radicals and ethylene. Mass-to-charge ratios (m/z) as indicated. The asterisks (*) mark radical species. c) Temperature dependence of partial pressure ratio of ethyl radicals (m/z=29) and ethylene (m/z=28) to unfragmented DES (m/z=90) monitored by *in situ* mass spectroscopy (left axis) and I_C/I_{Si} Raman integral ratio as indicator of deposited carbon (right axis), as extracted from a). d) Effect of H_2 on the partial pressure ratio of ethylene to unfragmented DES.

To better understand the decomposition mechanism of DES, we have investigated the onset and degree of pyrolysis via *in situ* mass spectroscopy, by monitoring the partial pressure of DES and its main pyrolysis fragments as a function of growth temperature (Figure S15). Figure 4b illustrates unimolecular dissociation as an important pathway of the DES pyrolysis mechanism.[37] In the mass spectroscopy fragmentation pattern (Figure S15) the unfragmented, single charged molecular ion of DES appears at mass-to-charge ratio of m/z=90. The dissociation is initiated at the C-S bond and involves the production of ethyl radicals (m/z=29), which further decompose to the more thermally stable ethylene (m/z=28) after H abstraction.[74] The partial pressure ratios of these pyrolysis products relative to the unfragmented DES species are displayed in Figure 4c (left axis) and can be used to monitor the pyrolysis degree. The ethyl radical/DES and ethylene/DES ratios start to exponentially increase at around 600ºC, marking the onset of DES pyrolysis initiated by H effusion around this temperature.[75] Importantly, the pyrolysis onset coincides with the onset of the deposited C amount, as extracted from *ex situ* Raman analysis of the I_C/I_{Si} integral ratio (Figure 4c, right axis). This correlation gives strong support to the hypothesis that C-containing products, resulting from the thermally activated gas-phase decomposition of DES along the hot-wall reactor tube, lead to the formation of graphitic C exhibiting a temperature-dependent rate. In contrast, *Choudhury et al.*,[24] while using a cold-wall reactor for WS_2 growth from DES, found a rather constant C formation rate over a wide range of temperatures, which is most probably due to reduced, premature DES pyrolysis upstream the sample in the case of a cold-wall system.[24] Moreover, *Choudhury et al.*[24] speculated that the reason of C-reduced MoS_2 growth from DES using a hot-wall reactor in the work of Kang *et al.*[17] was a result of early depletion of C radicals and C deposition on upstream tube walls. However, our investigation suggests that Kang *et al.* avoided C incorporation by choice of a comparatively low growth temperature of 550ºC and additional use of reductive H_2 (as discussed in Section 2.4, below). This highlights the importance of growth temperature and reactor design when an organic chalcogen precursor is used.

After the DES single source experiment, we then monitored the temperature dependent DES pyrolysis degree for a gas mixture of 1.2 sccm DES co-injected with 0.02 sccm $Mo(CO)_6$, as used for MoS_2 growth (Figure 4d, black line). We observed that the DES pyrolysis onset shifted to lower temperatures (around 500ºC). This suggests the $Mo(CO)_6$ catalyzed DES pyrolysis, as previously reported.[36] Our finding is further confirmed by a systematic increase in C deposition on SiO_2 substrates exposed to both DES and $Mo(CO)_6$ when compared to those only exposed to DES (Figures S17 and S18).

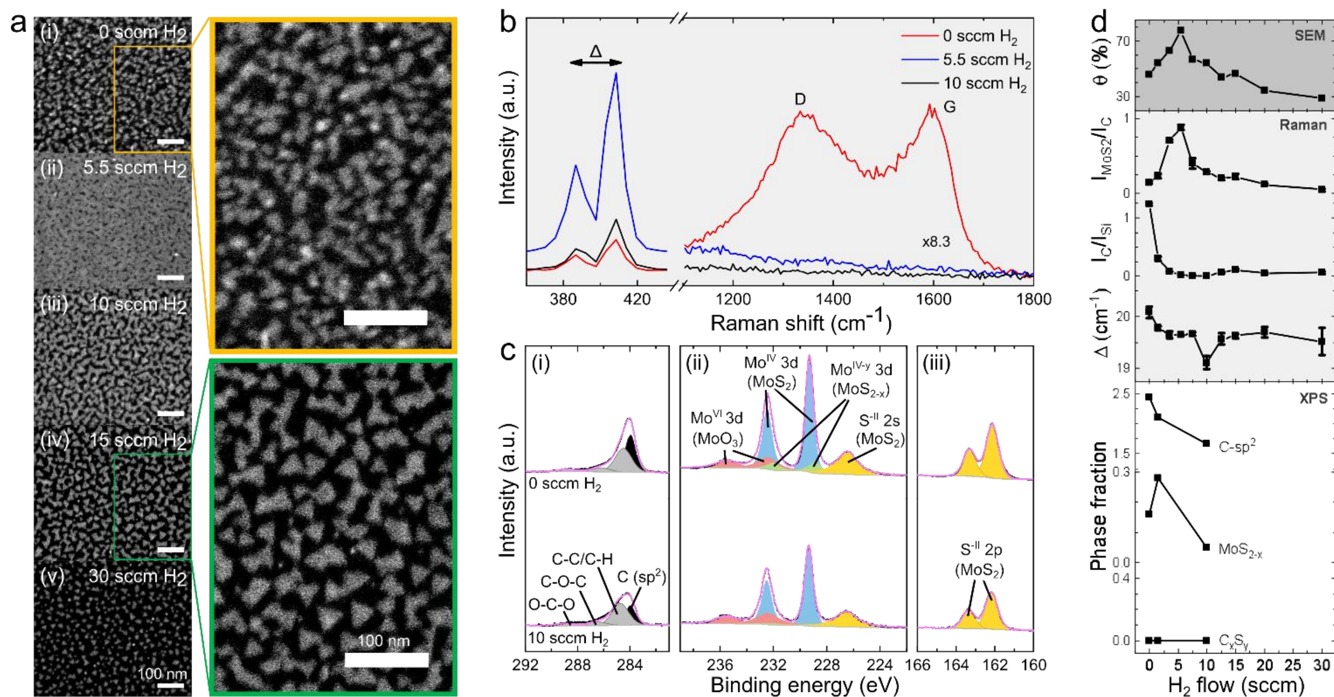

Figure 5. Effect of H_2 on MoS_2 thin films grown at 700°C (60 min) from 0.02 sccm $Mo(CO)_6$, 1.2 sccm DES flow and H_2 flow varying between 0 and 30 sccm. a(i-v) SEM images for different H_2 flows, as indicated in the figures. The insets show magnified images for better visualization of the grain morphology. b) Raman spectra normalized to Si peak (521 cm^{-1}, not shown) for 0 sccm (red), 5.5 sccm (green), and 10 sccm (black) H_2 flow. C-related D and G bands are magnified by a factor of 8.3. c(i-iii) XPS spectra for 0 sccm (top) and 10 sccm (bottom) H_2 flow of the C 1s, Mo 3d/ S 2s and S 2p core levels; colored areas under singlet/doublet peaks represent fits assigned to the same chemical compound and pink lines show the fitting envelopes of summed peaks. d) Summary of film characteristics as a function of the H_2 flow, extracted from SEM (coverage θ), Raman spectroscopy (I_{MoS2}/I_{Si} and I_C/I_{Si} integral ratios, and $\Delta(A_{1g} - E^1_{2g})$ frequency difference) and XPS (sp^2-C, MoS_{2-x} and C_xS_y fractions normalized to MoS_2-related Mo^{IV} $3d_{5/2}$ peak).

3.4 Effect of H_2 on DES pyrolysis, MoS_2 growth and C reduction

While low growth temperatures are a viable option to reduce C incorporation, high growth temperatures have been demonstrated as ideal for the deposition of high crystalline quality TMDs.[11, 35, 49] To this end, the use of H_2 gas has been proposed to reduce C incorporation in TMDs grown at high temperature regimes from organic chalcogen sources.[17, 22, 24, 35] We first investigated the effect of H_2 added to the $Mo(CO)_6$:DES mixture on the temperature-dependent DES pyrolysis via *in situ* gas-phase monitoring. Using ethylene as the main indicator, it was observed that H_2 introduction significantly lowered the partial pressure of DES pyrolysis products (Figure 4d, Figure S15), indicating a reduced DES pyrolysis degree even above 700ºC. This result suggests that a H_2-rich gas phase effectively suppresses DES dissociation, possibly by counterbalancing the H-abstraction mechanisms that initiate DES pyrolysis.[37]

Once the effect of H_2 on DES pyrolysis was assessed, we performed a series of MoS_2 growths varying H_2 flow from 0 to 30 sccm, while keeping constant the DES flow at 1.2 sccm, the $Mo(CO)_6$ flow at 0.02 sccm, temperature at 700°C, and growth time at 60 min. From SEM images (Figure 5a) and analysis (Figure 5d, 'SEM'), it is observed that the MoS_2 surface coverage initially increases, from 46% (0 sccm H_2) to a maximum of 77% (5.5 sccm), and subsequently declines monotonically for H_2 flows above 5.5 sccm, while maintaining a roughly constant nucleation density across all H_2 flows (Figure S9). This shows improved layer coalescence for an optimized H_2 flow. The I_{MoS_2}/I_{Si} Raman integral ratio (Figure 5d, 'Raman', top), follows the coverage dependence with H_2, corroborating with the SEM analysis. The initial increase in MoS_2 film coverage also correlates well with the decrease of I_C/I_{Si} (Figure 5d, 'Raman', middle), which can be explained by the enhanced lateral growth of MoS_2 domains due to removal of the growth-hindering C contamination. This promoted lateral 2D growth mode is confirmed by the decrease of the frequency shift $\Delta(A_{1g} - E^1_{2g})$ (Figure 5d, 'Raman', bottom), indicating a decrease in MoS_2 layer thickness with increasing H_2; $\Delta(A_{1g} - E^1_{2g})$ drops from about 20.1 cm^{-1} to around 19.6 cm^{-1}, as lateral MoS_2 grain growth becomes thermodynamically favored over vertical few layer nucleation on the C contamination-reduced high-energy SiO_2 surface.[59] The SEM images also indicate the reduction of the second layer nucleation: the white contrast spots on top of the grey primary layer MoS_2 domains disappear upon adding H_2 (see Figure S7 for the full set of SEM images).

Additionally, the MoS_2 grain shape was observed to change gradually from irregular/roundish to a triangular shape upon increasing H_2, as revealed by the insets in Figure 5a and by the complete set of SEM images for the H_2

series in the Supporting Information (Figure S7). The irregular grain shape in absence of H_2 hints at disturbed crystallinity due to the use of an organic sulfiding agent.[20, 21] Although our post-growth XPS analysis (Figure 5c) did not confirm C-Mo bondings (i.e. incorporation of C into the MoS_2 crystal domains), it is possible that intermediate MoS_xC_y edge compounds[21, 42, 43] play a role during attachment of S species at the catalytically active edges of the laterally growing MoS_2 crystal. This could in turn hinder the ideal S dimer saturation of the Mo-terminated edge that is preferred in triangular MoS_2 crystals.[45] As known from hydrodesulfurization catalysts, such "deactivation" of edge sites through carbonaceous species can be recovered in H_2 ambient[76] and might explain our observed shape evolution towards preferred triangular grain growth at increased H_2 flow. On the other hand, excessive H_2 flow above 5.5 sccm results in decreasing grain coverage at constant nucleation density. This implies reduced lateral MoS_2 growth rate, which we attribute to H_2-induced etching of domain edges.[17, 25, 29] Indeed, Raman analysis of the I_{MoS2}/I_{Si} ratio for growth time studies with and without H_2 confirm lowered growth rates in presence of H_2 (Figure S17a(ii)). Thus, by increasing H_2 flow, longer growth times are required for similar coverages, which was demonstrated in a growth parameter study for two sets of H_2 flows (growth times) of 5.5 sccm (60 min growth) and 12.5 sccm (180 min), which is presented in Figure S8 and Figure S9d.

Figure 5c(ii) shows XPS analysis of films grown without and with 10 sccm H_2, which present Mo^{IV} 3d doublets and S^{-II} 2p doublets ascribed to MoS_2, as well as Mo^{VI} 3d doublets assigned to MoO_3. A lower fraction of substoichiometric MoS_{2-x} phase is observed for the 10 sccm H_2 sample (Figure 5d, 'XPS', middle) and might be due to an optimized edge sulfidation mechanism. Further, compared to the H_2-free growth, the 10 sccm H_2 sample exhibits a lower C incorporation, confirmed by a decreased C(sp^2) fraction (as seen in the C 1s spectra in Figure 5c(i) and analyzed in Figure 5d, 'XPS', top). However, in contrast to the fully diminished Raman D and G band signature (Figure 5b), a residual XPS C 1s fraction is noticed for the 10 sccm H_2 condition. This observation suggests that even though graphitic C(sp^2) can be significantly reduced in H_2-ambient, residual C impurities, which need further investigation, might still remain in the film.

3.5 MoS_2 photoluminescence and C doping

In the previous sections we have demonstrated how fine tuning of growth parameters (e.g. DES or H_2 flow) allows precise control over film morphology (i.e. coverage θ) and C impurity levels (i.e. I_C/I_{Si}). To understand how these parameters affect the (opto)electronic properties of these films, we have performed PL spectroscopy. As illustrated in Figure 6a, laser excitation (488 nm, 2.54 eV) above the optical bandgap of monolayer MoS_2 results in two pronounced PL absorption features associated to neutral A^o and B excitons at around 1.89 eV and 2.04 eV, respectively. These excitons arise from direct optical transitions from the highest spin-split valence bands due to spin-orbit coupling (SOC) within the electronic bandgap E_g at the K (K') point of the Brillouin zone.[2] They can be understood as bound electron-hole pairs with a binding energy E_b^E in the quasi-particle model. Additionally, negatively charged trions A^-, three-body quasi-particles consisting of a hole and two electrons with trion binding energy E_b^T, may occur as a consequence of increased electron density in MoS_2.[77, 78]

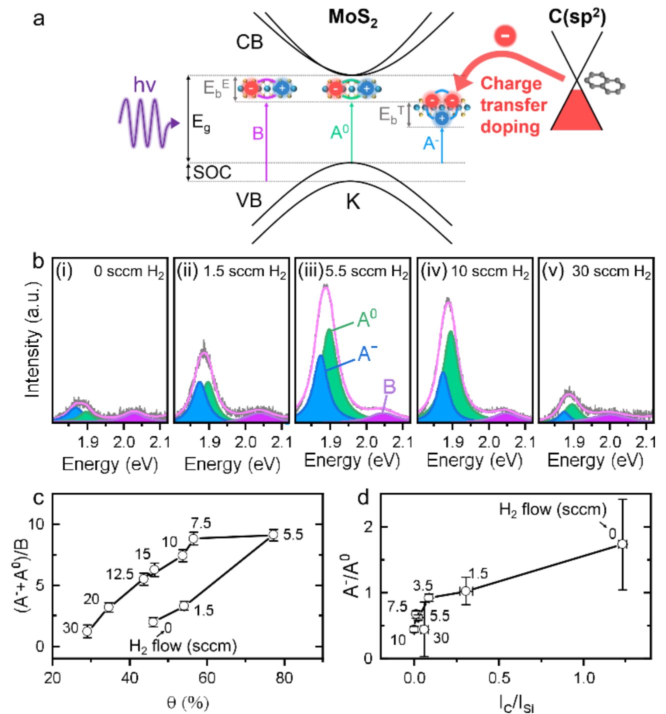

Figure 6. MoS_2 photoluminescence and charge transfer doping. a) Schematic representation of the electronic band structure of MoS_2 at the K point with electronic bandgap E_g between the conduction band (CB) and valence band (VB). The VB is spin-split due to spin-orbit coupling (SOC). Laser irradtion excites neutral A^o and B excitons with binding energy E_b^E and negative trions with binding energy E_b^T. Negative charge transfer from graphitic C(sp^2) in contact with MoS_2 induces trion formation. b)(i-v) PL spectra of MoS_2 thin films grown at 700°C (60 min) from 0.02 sccm $Mo(CO)_6$, 1.2 sccm DES flow and different H_2 flows varying between 0 and 30 sccm, as indicated. Lorentzian peak deconvolution marks contributions of trions A^- (blue), neutral excitons A^o (green) and B excitons (purple). The fitting envelopes are shown by the pink lines. Spectra are normalized to the B exciton intensity. c) PL integral ratio $(A^-+A^o)/B$ as function of coverage θ for MoS_2 films grown with different H_2 flows, as indicated next to each measurement point. d) Trion-to-exciton ratio A^-/A^o as function of graphitic C content, represented by I_C/I_{Si} Raman integral ratio, for MoS_2 films grown with different H_2 flows, as indicated next to each measurement point.

Figure 6b shows the PL spectra of MoS_2 films grown with different H_2 flows from the previous Section 2.4, fitted with

their respective A^o, B and A^- contributions. First, we observed that the PL intensity normalized to the B exciton intensity, considering the $(A^-+A^o)/B$ integral ratio as a quality factor,[53] correlates with the varying film coverage as function of H_2 flow (Figure S20), and reaches a maximum for the highest coverage of the 5.5 sccm H_2 sample. This overall PL intensity behavior governed by the surface coverage (grain size) dependence[79] was also observed for films grown with varied DES flow (Figure S21); larger monolayer coverages (larger grain sizes) generally result in stronger A exciton peak intensity due to enhanced A exciton recombination lifetimes and reduced non-radiative recombination channels.[79] Interestingly, when plotting the $(A^-+A^o)/B$ intensity ratio as a function of coverage (Figures 6c), we do not observe a solely monotonic coverage dependence. Instead, two branches appear for films grown with H_2 flows below and above 5.5 sccm, which belong to films with high and reduced amount of C impurities, respectively, as discussed in Section 2.4. For example, films grown with 0 sccm and 10 sccm show similar coverages, but differ in $(A^-+A^o)/B$ intensity ratio by almost an order of magnitude. Therefore, the reduced PL intensity in the sample grown without H_2 can be explained by its high C(sp^2) content. These results confirm that the presence of C(sp^2) results in strong PL quenching under illumination, as has been observed in MoS_2/graphene heterostructures.[48, 80] This phenomenon has been explained by charge transfer at the MoS_2/C(sp^2) heterointerface[81] and hints at electronic doping of MoS_2 in presence of C impurities.[48] However, we note that in the literature both n-type[48, 81] and p-type[80] doping of MoS_2 in interface with C(sp^2) have been discussed controversially.

To confirm the hypothesis of the doping effect, a closer look is taken at the A exciton peak. The Lorentzian peak deconvolution reveals that the A exciton peak consists of the neutral A^o exciton and charged A^- trion, which we find separated by the trion binding energy $E_b{}^T$ of around 20 – 30 meV consistent with literature.[51, 77] As the appearance of the trion is induced by an increased negative charge density within the MoS_2 layer, a prominent A^- weight and increased A^-/A^o ratio are indicators for electron doping.[47, 48, 77, 78] All our films in this H_2 series show A^-/A^o ratios above around 0.5 (Figure 6d), which can be attributed to various trion-inducing doping effects, such as S vacancies, strain, or the pronounced effect of charged impurities at the MoS_2/SiO_2 interface.[78] However, it is remarkable that the A^-/A^o ratio is increasing with increased I_C/I_{Si} ratio as a consequence of reducing the H_2 flow (Figure 6d). In other words, as the C content increases, the MoS_2 monolayer becomes more *n*-type and the trion-related PL dominates the spectra. This trend was also found for films with increasing C content controlled by the DES flow (Figure S21d). Moreover, a Stokes redshift of PL emission peaks in the range of 10 – 30 meV was observed with increasing C content (Figure S22), further supporting the hypothesis of the *n*-type doping of MoS_2 controlled by C impurity levels.[77] From an electrostatic point-of-view, the doping of MoS_2 can be explained by a negative charge transfer from donor states of nanographitic C(sp^2) located within the bandgap of MoS_2, as proposed in the band diagram model in Figure 6a.[46, 48] This band line-up is supported by X-ray and ultra-violet photoemission spectroscopy (XPS/UPS) studies; further discussion is provided in the Supporting Information (Figure S23).

3.6 Discussion of growth model

As summary of our results from the previous sections and to explain the interplay between the DES pyrolysis-induced reaction pathway and MoS_2 growth (and C co-deposition), we propose the following, simplified reaction scheme:

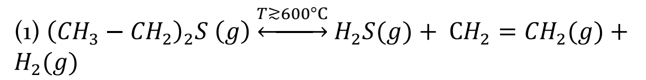

(1) $(CH_3-CH_2)_2S\ (g) \xleftrightarrow{T\gtrsim 600°C} H_2S(g) + CH_2 = CH_2(g) + H_2(g)$

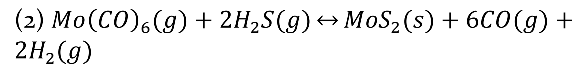

(2) $Mo(CO)_6(g) + 2H_2S(g) \leftrightarrow MoS_2(s) + 6CO(g) + 2H_2(g)$

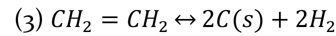

(3) $CH_2 = CH_2 \leftrightarrow 2C(s) + 2H_2$

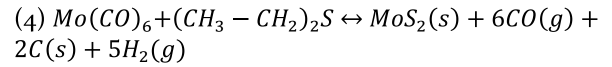

(4) $Mo(CO)_6 + (CH_3-CH_2)_2S \leftrightarrow MoS_2(s) + 6CO(g) + 2C(s) + 5H_2(g)$

For simplicity, we assume full conversion of DES to H_2S and ethylene (1), which were main gas-phase constituents detected by mass spectroscopy (Figure S15). We note that there are also other intermediate, radical fragments from DES pyrolysis (e.g. ethyl radicals) present in the gas-phase. H_2S is consumed in the sulfidation reaction (2) for the synthesis of MoS_2; and ethylene decomposition (3) acts as a source of C.[82] If H_2 is added to the gas phase, the equilibrium of all reactions will shift to the left side, thus resulting in suppressed DES pyrolysis in reaction (1) and reduced C incorporation in reaction (3). However, high H_2 concentration in reaction (2) can also lower the growth rate of MoS_2, as discussed in Section 3.4. The reaction pathway (1), which normally requires temperatures above the DES pyrolysis onset ≳600°C, see Figure 4c, can even occur at lower temperatures in presence of $Mo(CO)_6$ (Figure 4d), possibly due to surface-templated reactions on the SiO_2 substrate[83] and hydrodesulfurization of DES at the catalytically active edge sites of growing MoS_2,[44] as discussed in Section 3.4. Reaction (4) is the sum of reactions (1), (2) and (3).

While this study focuses on the growth of monolayer MoS_2, our results are aligned with previous works on the MOCVD of WSe_2[35, 36] and WS_2.[24] Current understanding of the MOCVD growth of 2D TMDs typically highlights the importance of high chalcogen-to-metal ratios for optimal

sulfidation,[24, 35] which is also suggested by our XPS stoichiometry study (Figure 3(c-d)). However, in the case of organic chalcogen precursors a high chalcogen-to-metal ratios can lead to co-deposition of C(sp^2), which in turn impedes the lateral growth of 2D TMD crystals, in agreement with literature.[24, 36] So far, it has been widely neglected to study the root-cause mechanisms and effects of C incorporation during MOCVD growth. Previous works speculated that C incorporation is caused by organic chalcogen precursor pyrolysis, but did not show experimental evidence. Our work confirms this hypothesis by combining *in situ* gas-phase monitoring together with post-growth, semi-quantitative Raman analysis. We have been able to correlate the degree of thermally activated chalcogen precursor pyrolysis with the C impurity level in as-grown films. Moreover, we have discussed this phenomenon in the context of the growth temperature and the reactor design (i.e. hot-wall compared to cold-wall configuration).[24] When using H_2 for mitigation of C incorporation, as proposed in previous works,[17, 24, 35, 36] we emphasize on the careful adjustment of H_2 flow to limit H_2-induced etching[25] and to control MoS_2 growth rate and surface coverage for improved film coalescence and continuity.

IV. Conclusions

The influence of synthesis parameters (i.e. temperature, chalcogen-to-metal ratio, H_2 flow) during MOCVD of polycrystalline, monolayer MoS_2 thin films on SiO_2 from the precursors $Mo(CO)_6$ and DES was investigated in a hot-wall reactor by *in situ* gas-phase monitoring (mass spectroscopy) combined with *ex situ* film analyses (SEM, AFM, Raman, XPS, PL). It was revealed that DES pyrolysis is involved in the production of C-containing gas-phase species via an unimolecular dissociation mechanism; this causes co-deposition of nanographitic C(sp^2) at growth temperatures above DES pyrolysis onset and high chalcogen-to-metal ratios. The C incorporation was found to compete with and hinder the lateral growth of MoS_2 domains, which results in interrupted film morphology and imposes a limitation on the use of high chalcogen-to-metal ratios, which are desirable for the growth of stoichiometric MoS_2 films. Furthermore, the introduced C impurities lead to *n*-doping of MoS_2, suggesting charge transfer at the MoS_2/C(sp^2) heterointerface. By adding H_2 to the gas-phase we demonstrate that this reducing agent is effective in suppressing DES pyrolysis, thus, allowing precise control of C impurity incorporation, morphology, and photoluminescence of the MoS_2 film.

In summary, this work contributes important insights to gas-phase chemistry and synthesis conditions in the scalable MOCVD of 2D semiconductors. Our findings underline the challenges of high-quality 2D TMDs from low-cost, low toxicity organic chalcogen precursors. We highlight opportunities to engineer 2D semiconductors by a fine-tuned growth process, which can have wider implications for the performance of (opto)electronic devices.

ASSOCIATED CONTENT

The Supporting Information is available free of charge at [link] MOCVD reactor setup and growth process; Precursor flow estimation; SEM image analyses of growth parameter series; AFM analysis of lateral-to-vertical growth transition in presence of C; XPS analysis and peak fitting, differentiation between adventitious C and growth-induced sp^2-C; DES and $Mo(CO)_6$ single source exposure experiments; Vacuum background diagnosis; DES fragmentation pattern and temperature dependent pyrolysis, suppression of DES pyrolysis upon adding H_2; Raman spectra of growth parameter studies (temperature, growth time, DES flow, $Mo(CO)_6$ flow, H_2 flow) and analyses of I_{MoS_2}/I_{Si} and I_C/I_{Si} ratios and frequency difference $\Delta(A_{1g}-E^1_{2g})$; PL analysis and peak fitting, PL spectra of DES flow series and analysis of $(A^- + A^0)/B$ and A^-/A^0 ratios; XPS/UPS analysis of MoS_2/C/SiO_2 heterointerface band structure.

AUTHOR INFORMATION

Corresponding Author

*E-mail: joseantonio.garrido@icn2.cat

Present Addresses

† J. B.: DiamFab SAS, 38042 Grenoble Cedex 9, France
# C. H.: Inserm and Université Grenoble Alpes, 38400 Saint Martin d'Hères, France

Author Contributions

The manuscript was prepared through contributions of all authors:

C.M.S. – Investigation, conceptualization, MoS_2 growth, SEM, AFM, Raman, PL, mass spectroscopy measurements, formal analysis, writing - original draft; **J.M.C.R.** – Resources (technical support in design and installation of home-built reactor setup); **G.S.** – XPS measurements, review of XPS analysis; **J.B.** Writing - review & editing; **C.H.** – Writing - review & editing; **J.R.S.** – Conceptualization, writing - review & editing; **A.P.T.** Writing - review & editing, formal analysis; **J.S.** – Supervision, writing - review & editing; **E.d.C.** – Conceptualization, writing, review & editing, formal analysis; **J.A.G.** - Supervision, writing - review & editing, project administration, funding acquisition.

All authors have given approval to the final version of the manuscript.

Notes

The authors declare no competing financial interest.

ACKNOWLEDGMENT

This work was funded by the European Union's Horizon 2020 research and innovation programme (BrainCom, grant No. 73203, Nanosmart, grant No. 825213 and Graphene Flagship Core 3, grant No. 881603). We also acknowledge funding from Generalitat de Catalunya (2017 SGR 1426), and the 2DTecBio

(FIS2017-85787-R) funded by the Spanish Ministry of Science, Innovation and Universities, the Spanish Research Agency (AEI) and the European Regional Development Fund (FEDER/UE). The ICN2 is funded by the CERCA programme / Generalitat de Catalunya and supported by the Severo Ochoa Centres of Excellence programme, funded by the Spanish Research Agency (AEI, grant no. SEV-2017-0706).

C. M. S. acknowledges that this work has been done within the framework of the Ph.D. program in Materials Science of the Autonomous University of Barcelona. Further, C.M.S. wants to thank Anh Tuan Hoang for fruitful discussions.

ABBREVIATIONS

MOCVD, metal-organic chemical vapor deposition; 2D, two-dimensional; TMD, transition-metal dichalcogenide; DES, diethyl sulfide; FWHM, full-width-at-half-maximum; SEM, scanning electron microscopy; AFM, atomic force microscopy; PL, photoluminescence; XPS, X-ray photoelectron spectroscopy; CB, conduction band; VB, valence band; SOC, spin-orbit coupling; UPS, ultraviolet photoelectron spectroscopy.

REFERENCES

1. Das, S.; Robinson, J. A.; Dubey, M.; Terrones, H.; Terrones, M., Beyond Graphene: Progress in Novel Two-Dimensional Materials and van der Waals Solids. *Annual Review of Materials Research* **2015,** *45* (1), 1-27.
2. Mak, K. F.; Lee, C.; Hone, J.; Shan, J.; Heinz, T. F., Atomically Thin MoS2: A New Direct-Gap Semiconductor. *Phys. Rev. Lett.* **2010,** *105* (13), 4.
3. Splendiani, A.; Sun, L.; Zhang, Y. B.; Li, T. S.; Kim, J.; Chim, C. Y.; Galli, G.; Wang, F., Emerging Photoluminescence in Monolayer MoS2. *Nano Lett.* **2010,** *10* (4), 1271-1275.
4. Radisavljevic, B.; Radenovic, A.; Brivio, J.; Giacometti, V.; Kis, A., Single-layer MoS2 transistors. *Nature Nanotechnology* **2011,** *6* (3), 147-150.
5. Marega, G. M.; Zhao, Y. F.; Avsar, A.; Wang, Z. Y.; Tripathi, M.; Radenovic, A.; Kis, A., Logic-in-memory based on an atomically thin semiconductor. *Nature* **2020,** *587* (7832), 72-77.
6. Sangwan, V. K.; Lee, H.-S.; Bergeron, H.; Balla, I.; Beck, M. E.; Chen, K.-S.; Hersam, M. C., Multi-terminal memtransistors from polycrystalline monolayer molybdenum disulfide. *Nature* **2018,** *554* (7693), 500-504.
7. Mennel, L.; Symonowicz, J.; Wachter, S.; Polyushkin, D. K.; Molina-Mendoza, A. J.; Mueller, T., Ultrafast machine vision with 2D material neural network image sensors. *Nature* **2020,** *579* (7797), 62-66.
8. Zhang, X.; Grajal, J.; Vazquez-Roy, J. L.; Radhakrishna, U.; Wang, X. X.; Chern, W.; Zhou, L.; Lin, Y. X.; Shen, P. C.; Ji, X.; Ling, X.; Zubair, A.; Zhang, Y. H.; Wang, H.; Dubey, M.; Kong, J.; Dresselhaus, M.; Palacios, T., Two-dimensional MoS2-enabled flexible rectenna for Wi-Fi-band wireless energy harvesting. *Nature* **2019,** *566* (7744), 368–372.
9. Schneider, D. S.; Grundmann, A.; Bablich, A.; Passi, V.; Kataria, S.; Kalisch, H.; Heuken, M.; Vescan, A.; Neumaier, D.; Lemme, M. C., Highly Responsive Flexible Photodetectors Based on MOVPE Grown Uniform Few-Layer MoS2. *ACS Photonics* **2020,** 7 (6), 1388–1395.
10. Choi, M.; Bae, S. R.; Hu, L.; Hoang, A. T.; Kim, S. Y.; Ahn, J. H., Full-color active-matrix organic light-emitting diode display on human skin based on a large-area MoS2 backplane. *Sci. Adv.* **2020,** *6* (28), 6.
11. Lin, Y. C.; Jariwala, B.; Bersch, B. M.; Xu, K.; Nie, Y. F.; Wang, B. M.; Eichfeld, S. M.; Zhang, X. T.; Choudhury, T. H.; Pan, Y.; Addou, R.; Smyth, C. M.; Li, J.; Zhang, K. H.; Haque, M. A.; Folsch, S.; Feenstra, R. M.; Wallace, R. M.; Cho, K.; Fullerton-Shirey, S. K.; Redwing, J. M.; Robinson, J. A., Realizing Large-Scale, Electronic-Grade Two-Dimensional Semiconductors. *ACS Nano* **2018,** *12* (2), 965-975.
12. Backes, C.; et.; al., Production and processing of graphene and related materials. *2d Materials* **2020,** *7* (2), 282.
13. Thompson, A. G., MOCVD technology for semiconductors. *Mater. Lett.* **1997,** *30* (4), 255-263.
14. Lee, D. H.; Sim, Y.; Wang, J.; Kwon, S. Y., Metal-organic chemical vapor deposition of 2D van der Waals materials-The challenges and the extensive future opportunities. *APL Mater.* **2020,** *8* (3), 18.
15. Kalanyan, B.; Kimes, W. A.; Beams, R.; Stranick, S. J.; Garret, E.; Kalish, I.; Davydov, A. V.; Kanjolia, R. K.; Maslar, J. E., Rapid Wafer-Scale Growth of Polycrystalline 2H-MoS2 by Pulsed Metal-Organic Chemical Vapor Deposition. *Chem. Mat.* **2017,** *29* (15), 6279-6288.
16. Seol, M.; Lee, M. H.; Kim, H.; Shin, K. W.; Cho, Y.; Jeon, I.; Jeong, M.; Lee, H. I.; Park, J.; Shin, H. J., High-Throughput Growth of Wafer-Scale Monolayer Transition Metal Dichalcogenide via Vertical Ostwald Ripening. *Advanced Materials* **2020,** *32* (42), 8.
17. Kang, K.; Xie, S. E.; Huang, L. J.; Han, Y. M.; Huang, P. Y.; Mak, K. F.; Kim, C. J.; Muller, D.; Park, J., High-mobility three-atom-thick semiconducting films with wafer-scale homogeneity. *Nature* **2015,** *520* (7549), 656-660.
18. Shinde, N. B.; Francis, B.; Rao, M. S. R.; Ryu, B. D.; Chandramohan, S.; Eswaran, S. K., Rapid wafer-scale fabrication with layer-by-layer thickness control of atomically thin MoS2 films using gas-phase chemical vapor deposition. *APL Mater.* **2019,** 7 (8), 8.
19. Maury, F., Recent trends in the selection of metal-organic precursors for MOCVD process. *J. Phys. IV* **1995,** 5 (C5), 449-463.
20. Tuxen, A.; Gobel, H.; Hinnemann, B.; Li, Z. S.; Knudsen, K. G.; Topsoe, H.; Lauritsen, J. V.; Besenbacher, F., An atomic-scale investigation of carbon in MoS2 hydrotreating catalysts sulfided by organosulfur compounds. *J. Catal.* **2011,** *281* (2), 345-351.
21. Fuchtbauer, H. G.; Tuxen, A. K.; Li, Z. S.; Topsoe, H.; Lauritsen, J. V.; Besenbacher, F., Morphology and Atomic-Scale Structure of MoS2 Nanoclusters Synthesized with Different Sulfiding Agents. *Top. Catal.* **2014,** 57 (1-4), 207-214.
22. Kumar, V. K.; Dhar, S.; Choudhury, T. H.; Shivashankar, S. A.; Raghavan, S., A predictive approach to CVD of crystalline layers of TMDs: the case of MoS2. *Nanoscale* **2015,** *7* (17), 7802-7810.
23. Dhar, S.; Kumar, V. K.; Choudhury, T. H.; Shivashankar, S. A.; Raghavan, S., Chemical vapor deposition of MoS2 layers from Mo-S-C-O-H system: thermodynamic modeling and validation. *Phys. Chem. Chem. Phys.* **2016,** *18* (22), 14918-14926.
24. Choudhury, T. H.; Simchi, H.; Boichot, R.; Chubarov, M.; Mohney, S. E.; Redwing, J. M., Chalcogen Precursor Effect on Cold-Wall Gas-Source Chemical Vapor Deposition Growth of WS2. *Cryst. Growth Des.* **2018,** *18* (8), 4357-4364.
25. Chiappe, D.; Ludwig, J.; Leonhardt, A.; El Kazzi, S.; Mehta, A. N.; Nuytten, T.; Celano, U.; Sutar, S.; Pourtois, G.; Caymax, M.; Paredis, K.; Vandervorst, W.; Lin, D.; De Gendt, S.; Barla, K.; Huyghebaert, C.; Asselberghs, I.; Radu, I., Layer-controlled epitaxy of 2D semiconductors: bridging nanoscale

phenomena to wafer-scale uniformity. *Nanotechnology* **2018,** *29* (42), 9.

26. Beauchamp, R. O.; Bus, J. S.; Popp, J. A.; Boreiko, C. J.; Andjelkovich, D. A.; Leber, P., A Critical Review of the Literature on Hydrogen Sulfide Toxicity. *CRC Critical Reviews in Toxicology* **1984,** *13* (1), 25-97.

27. Hoang, A. T.; Katiyar, A. K.; Shin, H.; Mishra, N.; Forti, S.; Coletti, C.; Ahn, J. H., Epitaxial Growth of Wafer-Scale Molybdenum Disulfide/Graphene Heterostructures by Metal-Organic Vapor-Phase Epitaxy and Their Application in Photodetectors. *Acs Applied Materials & Interfaces* **2020,** *12* (39), 44335-44344.

28. Fan, Y.; Nakanishi, K.; Veigang-Radulescu, V. P.; Mizuta, R.; Stewart, J. C.; Swallow, J. E. N.; Dearle, A. E.; Burton, O. J.; Alexander-Webber, J. A.; Ferrer, P.; Held, G.; Brennan, B.; Pollard, A. J.; Weatherup, R. S.; Hofmann, S., Understanding metal organic chemical vapour deposition of monolayer WS2: the enhancing role of Au substrate for simple organosulfur precursors. *Nanoscale* **2020,** *12* (43), 22234-22244.

29. Cun, H.; Macha, M.; Kim, H.; Liu, K.; Zhao, Y.; LaGrange, T.; Kis, A.; Radenovic, A., Wafer-scale MOCVD growth of monolayer MoS2 on sapphire and SiO2. *Nano Research* **2019,** (10), 2646-2652.

30. Zhao, R.; Lo, C. L.; Zhang, F.; Ghosh, R. K.; Knobloch, T.; Terrones, M.; Chen, Z. H.; Robinson, J., Incorporating Niobium in MoS2 at BEOL-Compatible Temperatures and its Impact on Copper Diffusion Barrier Performance. *Adv. Mater. Interfaces* **2019**, 7.

31. Jin, G.; Lee, C. S.; Liao, X.; Kim, J.; Wang, Z.; Okello, O. F. N.; Park, B.; Park, J.; Han, C.; Heo, H.; Kim, J.; Oh, S. H.; Choi, S. Y.; Park, H.; Jo, M. H., Atomically thin three-dimensional membranes of van der Waals semiconductors by wafer-scale growth. *Sci. Adv.* **2019,** *5* (7), 6.

32. Marx, M.; Grundmann, A.; Lin, Y. R.; Andrzejewski, D.; Kummell, T.; Bacher, G.; Heuken, M.; Kalisch, H.; Vescan, A., Metalorganic Vapor-Phase Epitaxy Growth Parameters for Two-Dimensional MoS2. *J. Electron. Mater.* **2018,** *47* (2), 910-916.

33. Grundmann, A.; Andrzejewaki, D.; Kummell, T.; Baoher, G.; Heuken, M.; Kalisch, H.; Vescan, A., H2S-free Metal-Organic Vapor Phase Epitaxy of Coalesced 2D WS2 Layers on Sapphire. *MRS Adv.* **2019,** *4* (10), 593-599.

34. Cohen, A.; Patsha, A.; Mohapatra, P. K.; Kazes, M.; Ranganathan, K.; Houben, L.; Oron, D.; Ismach, A., Growth-Etch Metal–Organic Chemical Vapor Deposition Approach of WS2 Atomic Layers. *ACS Nano* **2020,** *15* (1), 526-538.

35. Eichfeld, S. M.; Hossain, L.; Lin, Y. C.; Piasecki, A. F.; Kupp, B.; Birdwell, A. G.; Burke, R. A.; Lu, N.; Peng, X.; Li, J.; Azcatl, A.; McDonnell, S.; Wallace, R. M.; Kim, M. J.; Mayer, T. S.; Redwing, J. M.; Robinson, J. A., Highly Scalable, Atomically Thin WSe2 Grown via Metal-Organic Chemical Vapor Deposition. *ACS Nano* **2015,** *9* (2), 2080-2087.

36. Zhang, X. T.; Balushi, Z. Y.; Zhang, F.; Choudhury, T. H.; Eichfeld, S. M.; Alem, N.; Jackson, T. N.; Robinson, J. A.; Redwing, J. M., Influence of Carbon in Metalorganic Chemical Vapor Deposition of Few-Layer WSe2 Thin Films. *J. Electron. Mater.* **2016,** *45* (12), 6273-6279.

37. Zheng, X.; Fisher, E. M.; Gouldin, F. C.; Zhu, L.; Bozzelli, J. W., Experimental and computational study of diethyl sulfide pyrolysis and mechanism. *Proc. Combust. Inst.* **2009,** *32*, 469-476.

38. Song, J. G.; Ryu, G. H.; Kim, Y.; Woo, W. J.; Ko, K. Y.; Kim, Y.; Lee, C.; Oh, I. K.; Park, J.; Lee, Z.; Kim, H., Catalytic chemical vapor deposition of large-area uniform two-dimensional molybdenum disulfide using sodium chloride. *Nanotechnology* **2017,** *28* (46), 8.

39. Liang, T.; Habib, M. R.; Xiao, H.; Xie, S.; Kong, Y. H.; Yu, C.; Iwai, H.; Fujita, D.; Hanagata, N.; Chen, H. Z.; Feng, Z. H.; Xu, M. S., Intrinsically Substitutional Carbon Doping in CVD-Grown Monolayer MoS2 and the Band Structure Modulation. *ACS Appl. Electron. Mater.* **2020,** *2* (4), 1055-1064.

40. Zhang, F.; Lu, Y. F.; Schulman, D. S.; Zhang, T. Y.; Fujisawa, K.; Lin, Z.; Lei, Y.; Elias, A. L.; Das, S.; Sinnott, S. B.; Terrones, M., Carbon doping of WS2 monolayers: Bandgap reduction and p-type doping transport. *Sci. Adv.* **2019,** *5* (5), 8.

41. Cochrane, K. A.; Zhang, T.; Kozhakhmetov, A.; Lee, J. H.; Zhang, F.; Dong, C.; Neaton, J. B.; Robinson, J. A.; Terrones, M.; Bargioni, A. W.; Schuler, B., Intentional carbon doping reveals CH as an abundant charged impurity in nominally undoped synthetic WS2 and WSe2. *2d Materials* **2020,** *7* (3), 6.

42. Jeon, J.; Park, Y.; Choi, S.; Lee, J.; Lim, S. S.; Lee, B. H.; Song, Y. J.; Cho, J. H.; Jang, Y. H.; Lee, S., Epitaxial Synthesis of Molybdenum Carbide and Formation of a Mo2C/MoS2 Hybrid Structure via Chemical Conversion of Molybdenum Disulfide. *ACS Nano* **2018,** *12* (1), 338-346.

43. Kelty, S. P.; Berhault, G.; Chianelli, R. R., The role of carbon in catalytically stabilized transition metal sulfides. *Appl. Catal. A-Gen.* **2007,** *322*, 9-15.

44. Bruix, A.; Fuchtbauer, H. G.; Tuxen, A. K.; Walton, A. S.; Andersen, M.; Porsgaard, S.; Besenbacher, F.; Hammer, B.; Lauritsen, J. V., In Situ Detection of Active Edge Sites in Single-Layer MoS2 Catalysts. *ACS Nano* **2015,** *9* (9), 9322-9330.

45. Mom, R. V.; Louwen, J. N.; Frenken, J. W. M.; Groot, I. M. N., In situ observations of an active MoS2 model hydrodesulfurization catalyst. *Nature Communications* **2019,** *10*, 8.

46. Leonhardt, A.; Chiappe, D.; Afanas'ev, V. V.; El Kazzi, S.; Shlyakhov, I.; Conard, T.; Franquet, A.; Huyghebaert, C.; de Gendt, S., Material-Selective Doping of 2D TMDC through AlxOy Encapsulation. *Acs Applied Materials & Interfaces* **2019,** *11* (45), 42697-42707.

47. Mouri, S.; Miyauchi, Y.; Matsuda, K., Tunable Photoluminescence of Monolayer MoS2 via Chemical Doping. *Nano Lett.* **2013,** *13* (12), 5944-5948.

48. Li, Z.; Ye, R.; Feng, R.; Kang, Y.; Zhu, X.; Tour, J. M.; Fang, Z., Graphene Quantum Dots Doping of MoS2 Monolayers. *Advanced Materials* **2015,** *27* (35), 5235-5240.

49. Kim, H.; Ovchinnikov, D.; Deiana, D.; Unuchek, D.; Kis, A., Suppressing Nucleation in Metal-Organic Chemical Vapor Deposition of MoS2 Monolayers by Alkali Metal Halides. *Nano Lett.* **2017,** *17* (8), 5056-5063.

50. Schneider, C. A.; Rasband, W. S.; Eliceiri, K. W., NIH Image to ImageJ: 25 years of image analysis. *Nature Methods* **2012,** *9* (7), 671-675.

51. Lee, H. S.; Kim, M. S.; Kim, H.; Lee, Y. H., Identifying multiexcitons in MoS2 monolayers at room temperature. *Phys. Rev. B* **2016,** *93* (14), 6.

52. Cancado, L. G.; Takai, K.; Enoki, T.; Endo, M.; Kim, Y. A.; Mizusaki, H.; Jorio, A.; Coelho, L. N.; Magalhaes-Paniago, R.; Pimenta, M. A., General equation for the determination of the crystallite size L-a of nanographite by Raman spectroscopy. *Appl. Phys. Lett.* **2006,** *88* (16), 3.

53. McCreary, K. M.; Hanbicki, A. T.; Sivaram, S. V.; Jonker, B. T., A- and B-exciton photoluminescence intensity ratio as a measure of sample quality for trancition metal dichalcogenide monolayers. *APL Mater.* **2018,** *6* (11), 9.

54. Qin, B.; Ma, H.; Hossain, M.; Zhong, M.; Xia, Q.; Li, B.; Duan, X., Substrates in the Synthesis of Two-Dimensional

Materials via Chemical Vapor Deposition. *Chem. Mat.* **2020,** *32* (24), 10321-10347.
55. Ahn, C.; Park, Y.; Shin, S.; Ahn, J.-G.; Song, I.; An, Y.; Jung, J.; Kim, C. S.; Kim, J. H.; Bang, J.; Kim, D.; Baik, J.; Lim, H., Growth of Monolayer and Multilayer MoS2 Films by Selection of Growth Mode: Two Pathways via Chemisorption and Physisorption of an Inorganic Molecular Precursor. *ACS Applied Materials & Interfaces* **2021,** *13* (5), 6805-6812.
56. Jiang, Z. Q.; Huang, W. X., Comparative Investigation of Mo(CO)(6) Adsorption on Clean and Oxidized Si(111) Surfaces. *Chin. J. Chem. Phys.* **2011,** *24* (6), 729-734.
57. Usoltsev, I.; Eichler, R.; Wang, Y.; Even, J.; Yakushev, A.; Haba, H.; Asai, M.; Brand, H.; Di Nitto, A.; Dullmann, C. E.; Fangli, F.; Hartmann, W.; Huang, M.; Jager, E.; Kaji, D.; Kanaya, J.; Kaneya, Y.; Khuyagbaatar, J.; Kindler, B.; Kratz, J. V.; Krier, J.; Kudou, Y.; Kurz, N.; Lommel, B.; Miyashita, S.; Morimoto, K.; Morita, K.; Murakami, M.; Nagame, Y.; Nitsche, H.; Ooe, K.; Sato, T. K.; Schadel, M.; Steiner, J.; Steinegger, P.; Sumita, T.; Takeyama, M.; Tanaka, K.; Toyoshima, A.; Tsukada, K.; Turler, A.; Wakabayashi, Y.; Wiehl, N.; Yamaki, S.; Qin, Z., Decomposition studies of group 6 hexacarbonyl complexes. Part 1: Production and decomposition of Mo(CO)(6) and W(CO)(6). *Radiochim. Acta* **2016,** *104* (3), 141-151.
58. Xuan, Y.; Jain, A.; Zafar, S.; Lotfi, R.; Nayir, N.; Wang, Y.; Choudhury, T. H.; Wright, S.; Feraca, J.; Rosenbaum, L.; Redwing, J. M.; Crespi, V.; van Duin, A. C. T., Multi-scale modeling of gas-phase reactions in metal-organic chemical vapor deposition growth of WSe2. *J. Cryst. Growth* **2019,** *527*, 125247.
59. Shang, S. L.; Lindwall, G.; Wang, Y.; Redwing, J. M.; Anderson, T.; Liu, Z. K., Lateral Versus Vertical Growth of Two-Dimensional Layered Transition-Metal Dichalcogenides: Thermodynamic Insight into MoS2. *Nano Lett.* **2016,** *16* (9), 5742-5750.
60. Sitek, J.; Plocharski, J.; Pasternak, I.; Gertych, A. P.; McAleese, C.; Conran, B. R.; Zdrojek, M.; Strupinski, W., Substrate-Induced Variances in Morphological and Structural Properties of MoS2 Grown by Chemical Vapor Deposition on Epitaxial Graphene and SiO2. *ACS Applied Materials & Interfaces* **2020,** *12* (40), 45101-45110.
61. Lee, C.; Yan, H.; Brus, L. E.; Heinz, T. F.; Hone, J.; Ryu, S., Anomalous Lattice Vibrations of Single- and Few-Layer MoS2. *ACS Nano* **2010,** *4* (5), 2695-2700.
62. Lopez-Diaz, D.; Holgado, M. L.; Garcia-Fierro, J. L.; Velazquez, M. M., Evolution of the Raman Spectrum with the Chemical Composition of Graphene Oxide. *J. Phys. Chem. C* **2017,** *121* (37), 20489-20497.
63. Ferrari, A. C.; Robertson, J., Interpretation of Raman spectra of disordered and amorphous carbon. *Phys. Rev. B* **2000,** *61* (20), 14095-14107.
64. Wildervanck, J. C.; Jellinek, F., Preparation and Crystallinity of Molybdenum and Tungsten Sulfides. *Z. Anorg. Allg. Chem.* **1964,** *328* (5-6), 309-318.
65. Cadot, S.; Renault, O.; Fregnaux, M.; Rouchon, D.; Nolot, E.; Szeto, K.; Thieuleux, C.; Veyre, L.; Okuno, H.; Martin, F.; Quadrelli, E. A., A novel 2-step ALD route to ultra-thin MoS2 films on SiO2 through a surface organometallic intermediate. *Nanoscale* **2017,** *9* (2), 538-546.
66. Benck, J. D.; Chen, Z.; Kuritzky, L. Y.; Forman, A. J.; Jaramillo, T. F., Amorphous Molybdenum Sulfide Catalysts for Electrochemical Hydrogen Production: Insights into the Origin of their Catalytic Activity. *ACS Catal.* **2012,** *2* (9), 1916-1923.
67. Gao, J.; Li, B. C.; Tan, J. W.; Chow, P.; Lu, T. M.; Koratkar, N., Aging of Transition Metal Dichalcogenide Monolayers. *ACS Nano* **2016,** *10* (2), 2628-2635.
68. Kastl, C.; Chen, C. T.; Kuykendall, T.; Shevitski, B.; Darlington, T. P.; Borys, N. J.; Krayev, A.; Schuck, P. J.; Aloni, S.; Schwartzberg, A. M., The important role of water in growth of monolayer transition metal dichalcogenides. *2d Materials* **2017,** *4* (2), 10.
69. Baker, M. A.; Gilmore, R.; Lenardi, C.; Gissler, W., XPS investigation of preferential sputtering of S from MoS2 and determination of MoSx stoichiometry from Mo and S peak positions. *Appl. Surf. Sci.* **1999,** *150* (1-4), 255-262.
70. Kim, I. S.; Sangwan, V. K.; Jariwala, D.; Wood, J. D.; Park, S.; Chen, K. S.; Shi, F. Y.; Ruiz-Zepeda, F.; Ponce, A.; Jose-Yacaman, M.; Dravid, V. P.; Marks, T. J.; Hersam, M. C.; Lauhon, L. J., Influence of Stoichiometry on the Optical and Electrical Properties of Chemical Vapor Deposition Derived MoS2. *ACS Nano* **2014,** *8* (10), 10551-10558.
71. Levasseur, A.; Vinatier, P.; Gonbeau, D., X-ray photoelectron spectroscopy: A powerful tool for a better characterization of thin film materials. *Bull. Mat. Sci.* **1999,** *22* (3), 607-614.
72. Chang, C. H., Preparation and characterization of carbon-sulfur surface compounds. *Carbon* **1981,** *19* (3), 175-186.
73. Abdelkader-Fernandez, V. K.; Domingo-Garcia, M.; Lopez-Garzon, F. J.; Fernandes, D. M.; Freire, C.; de la Torre, M. D. L.; Melguizo, M.; Godino-Salido, M. L.; Perez-Mendoza, M., Expanding graphene properties by a simple S-doping methodology based on cold CS2 plasma. *Carbon* **2019,** *144*, 269-279.
74. Ivin, K. J.; Wijnen, M. H. J.; Steacie, E. W. R., Reactions of ethyl radicals. *J. Phys. Chem.* **1952,** *56* (8), 967-972.
75. Conway, N. M. J.; Ferrari, A. C.; Flewitt, A. J.; Robertson, J.; Milne, W. I.; Tagliaferro, A.; Beyer, W., Defect and disorder reduction by annealing in hydrogenated tetrahedral amorphous carbon. *Diam. Relat. Mat.* **2000,** *9* (3-6), 765-770.
76. Vogelaar, B. M.; Steiner, P.; van Langeveld, A. D.; Eijsbouts, S.; Moulijn, J. A., Deactivation of Mo/Al2O3 and NiMo/Al2O3 catalysts during hydrodesulfurization of thiophene. *Appl. Catal. A-Gen.* **2003,** *251* (1), 85-92.
77. Mak, K. F.; He, K. L.; Lee, C.; Lee, G. H.; Hone, J.; Heinz, T. F.; Shan, J., Tightly bound trions in monolayer MoS2. *Nature Materials* **2013,** *12* (3), 207-211.
78. Dubey, S.; Lisi, S.; Nayak, G.; Herziger, F.; Nguyen, V.-D.; Le Quang, T.; Cherkez, V.; González, C.; Dappe, Y. J.; Watanabe, K.; Taniguchi, T.; Magaud, L.; Mallet, P.; Veuillen, J.-Y.; Arenal, R.; Marty, L.; Renard, J.; Bendiab, N.; Coraux, J.; Bouchiat, V., Weakly Trapped, Charged, and Free Excitons in Single-Layer MoS2 in the Presence of Defects, Strain, and Charged Impurities. *ACS Nano* **2017,** *11* (11), 11206-11216.
79. Andrzejewski, D.; Marx, M.; Grundmann, A.; Pfingsten, O.; Kalisch, H.; Vescan, A.; Heuken, M.; Kummell, T.; Bacher, G., Improved luminescence properties of MoS2 monolayers grown via MOCVD: role of pretreatment and growth parameters. *Nanotechnology* **2018,** *29* (29), 10.
80. Pierucci, D.; Henck, H.; Naylor, C. H.; Sediri, H.; Lhuillier, E.; Balan, A.; Rault, J. E.; Dappe, Y. J.; Bertran, F.; Le Fevre, P.; Johnson, A. T. C.; Ouerghi, A., Large area molybdenum disulphide-epitaxial graphene vertical Van der Waals heterostructures. *Sci Rep* **2016,** *6*, 10.
81. Diaz, H. C.; Addou, R.; Batzill, M., Interface properties of CVD grown graphene transferred onto MoS2(0001). *Nanoscale* **2014,** *6* (2), 1071-1078.
82. Lin, L.; Lai, M. S.; Li, H. F.; Tian, F.; Chen, Y. L.; Sun, J. S.; Lin, J. M., Investigation of carbon deposition induced by pyrolytic decomposition of ethylene. *RSC Adv.* **2017,** *7* (47), 29639-29644.

83. Gao, F.; Wang, Y.; Tysoe, W. T., Ethylene hydrogenation on Mo(CO)6 derived model catalysts in ultrahigh vacuum: From oxycarbide to carbide to MoAl alloy. *Journal of Molecular Catalysis A: Chemical* **2006,** *249* (1), 111-122.

Table of Contents artwork